Highlights

- Large format pouch LFP cell full thermal characterisation of both surfaces.
- Wide range of ambient temperatures and C rates as expected in automotive industry.
- Gradients across the cell thickness can be larger than across the cell surface.
- Similar heat distribution between charge and discharge scenarios.
- Self heating increases available capacity at low temperatures

Large format lithium ion pouch cell full thermal characterisation for improved electric vehicle thermal management

Thomas Grandjean, Anup Barai, Elham Hosseinzadeh, Yue Guo, Andrew McGordon, James Marco

WMG, University of Warwick, Coventry, CV4 7AL, United Kingdom

Keywords: Lithium ion; Temperature gradient; Thermal management; Thermal characterisation; Battery thermal management system

Abstract

It is crucial to maintain temperature homogeneity in lithium ion batteries in order to prevent adverse voltage distributions and differential ageing within the cell. As such, the thermal behaviour of a large-format 20 Ah lithium iron phosphate pouch cell is investigated over a wide range of ambient temperatures and C rates during both charging and discharging. Whilst previous studies have only considered one surface, this article presents experimental results, which characterise both surfaces of the cell exposed to similar thermal media and boundary conditions, allowing for thermal gradients in-plane and perpendicular to the stack to be quantified. Temperature gradients, caused by self-heating, are found to increase with increasing C rate and decreasing temperature to such an extent that 13.4 ± 0.7% capacity can be extracted using a 10C discharge compared to a 0.5C discharge, both at -10°C ambient temperature. The former condition causes a 18.8 ± 1.1˚C in plane gradient and a 19.7 ± 0.8˚C thermal gradient perpendicular to the stack, which results in large current density distributions and local state of charge differences within the cell. The implications of these thermal and electrical inhomogeneities on ageing and battery pack design for the automotive industry are discussed.

1. Introduction

With ever increasing endorsement of legislation to reduce carbon emissions, such as the EU 2020 targets [1], and rapidly escalating concerns over local air pollution [2], the automotive industry is actively developing alternative technologies to reduce its dependence on fossil fuels [3]. Consequently, hybrid electric vehicles (HEVs), plug-in hybrid electric vehicles (PHEVs), and battery electric vehicles (BEVs) have gained attention in recent years [4]. Government bodies and legislative bodies continue to implement favourable policies such as financial subsidies and tax exemptions and reductions for environmentally friendly vehicles [5]. Lithium ion batteries have become the prevailing choice for modern electric vehicles (EVs) due to their relatively high energy and power densities, long cycle life, lack of memory effect, and low self-discharge rates [6].

The properties of lithium ion cells, such as impedance and capacity, depend strongly on variables such as operating temperature, state of charge (SOC), the current rate and the relaxation time [7–9]. Lithium ion batteries require organic electrolytes due to the wide operating voltage of the cell [10]. The electrolytes are based on combinations of linear and cyclic alkyl carbonates, which allow the use of lithium as the anodic active component and gives lithium ion batteries their high power and energy densities characteristics. However, these organic electrolytes have high flammability and volatility that pose serious safety issues as they can react with the active electrode materials to release significant heat and gas, such as carbon dioxide, vaporized electrolyte consisting of ethylene and/or propylene, and combustion products of organic solvents [10]. In addition to safety concerns, the temperature sensitivity of the conductivity of the organic electrolyte makes lithium ion battery properties, such as internal resistance, more temperature dependent than other types of batteries [11].

During usage, the performance of lithium ion batteries degrades and key characteristics, such as capacity and impedance, worsen due to ageing mechanisms, e.g. solid electrolyte interphase (SEI) layer growth [12–14]. Increased impedance is detrimental as less power can be extracted from the cell and additional heat is generated [15]. It is important for the cooling system to efficiently extract the extra heat produced. Experiments performed at different ambient temperatures have revealed that the ageing rate has a strong temperature dependence, often described by the Arrhenius equation [16–19]. Operating cells at elevated temperatures (>25˚C) is known to accelerate SEI film growth on the anode and degradation of the cathode, leading to capacity fade and increased internal impedance [19], the latter producing more heat

and accelerating ageing further in a positive feedback loop manner. The increased heat generation adds extra cooling requirements to the cooling system and may have catastrophic consequences such as thermal runaway if the cell temperature cannot be managed to an appropriate level throughout battery life for a range of different environmental conditions and use cases [10, 11, 20].

Significant thermal gradients may develop inside lithium-ion batteries during charging and discharging, which are more pronounced with increasing cell size and current rate [21–23]. Thermal gradients pose a significant challenge in lithium ion battery pack design [24], where it is crucial to maintain temperature homogeneity between the cells that constitute the battery pack in order to prevent adverse voltage distributions and differential ageing between the cells [25]. Consequently, manufacturers dedicate a large amount of resources to develop battery packs with corresponding thermal management systems, which aim to maintain each cell in identical thermal operating conditions [26]. These thermal management systems require accurate temperature sensing and comprehensive instrumentation of the battery system. However, commercial battery packs commonly have limited numbers of thermocouples to reduce cost, weight and computational complexity. For example the Toyota Prius and the Honda Civic Hybrid only have three thermistors for their battery packs consisting of 168 and 120 cells respectively [27], whilst the Nissan Leaf only has four temperature sensors for its 192 cell battery pack [28]. In the automotive industry, it is common practice for battery pack manufacturers to aim for a maximum 5˚C thermal gradient across the entire pack. Given that thermal gradients persist on the cell surface, the temperature measured by the battery management system (BMS) may not necessarily be the highest temperature on the cell surface and consequently poses a potential safety risk. It is therefore crucial to consider cell thermal gradients when designing lithium ion battery packs, instrumentation and their corresponding thermal management systems.

As a consequence of thermal gradients, the cell does not age uniformly and an ageing gradient occurs inside the cell [29, 30], reducing the efficiency and lifespan of lithium ion batteries. Strong thermal gradients can also lead to deformations of the jelly roll in cylindrical cells [22, 31]. The geometric orientation of the temperature gradient is also important: for a pouch cell, it has been shown that temperature gradients perpendicular to the stack layers lead to higher local currents and faster degradation compared to temperature gradients in-plane with the stack layers [26]. However, thermal gradients across the thickness of the cell have

been overlooked in the literature, since other studies on thermal gradients on large pouch cells [32–35] only consider one surface. The maximum temperature differences of a 16Ah NMC/graphite pouch cell surface has been reported to reach 2˚C, 4˚C and 10.5˚C for discharge C-rates of 1C, 3C and 8C, respectively [32]. A similar range of values for temperature gradients was recently reported for a 50 Ah NMC pouch cell: for 25˚C ambient a 2.5˚C and 5.5˚C cell surface difference at 3C and 6C discharge respectively, and for 0˚C ambient a 5.5˚C and 9˚C cell surface difference at 3C and 6C discharge respectively [33]. Smaller thermal gradients are observed on cylindrical cells since the metallic cell housing material has a high heat conductivity, e.g. for an 18650 high power NMC+LMO/graphite the maximum temperature difference on the cell surface is 0.8 ± 0.1˚C during a 1C discharge. This increases to 6.5 ± 0.1˚C if the same cell is discharged at a rate of 16C [32]. Similar behaviour has also been modelled in cylindrical LFP cells [36] and 16Ah LG Chem $LiMn_2O_4$ cathode/graphite anode pouch cells [34]. Due to developments in anode chemistry and composition these cells are can deliver large C rates [37, 38], e.g. 1-5C and 10-20C in EV and HEV applications respectively, and will be susceptible to thermal gradients. However, very few studies measure heat generation at high C rates (above 1C) [23] and often this is only performed at one [32, 35], sometimes two ambient temperatures [33]. Furthermore, no literature exits where two surfaces have been simultaneously instrumented.

Large pouch cells are currently used in production vehicles such as the Nissan Leaf, Renault Zoe, and Daimler Smart. The battery packs of EVs and HEVs deliver high power demand and accept high charge power at a wide temperature range from sub-zero to 40°C ambient conditions, and premature ageing of the battery packs has been reported in main-stream news media. The root cause of this premature ageing could be the temperature gradient, originate from high power demand. Despite the existing literature as mentioned earlier, indicating the persistence of temperature gradient and its implications on ageing and safety, a comprehensive study on large format cells with a wide range of temperatures and charge-discharge rates, matching with automotive application is currently not present in the literature.

In this study, the temperature gradients of commercially available large format pouch cells are investigated for a wide range of ambient temperatures and current rates commonly experienced in the automotive industry. Moreover, this study investigates the temperature gradients across the cell surface (in line with the stack) and across the cell thickness

(perpendicular to the stack), which has been overlooked in the literature. Furthermore, this study analyses both charge and discharge, where previous studies have only considered discharge.

The outcome of the research presented is intended to improve understanding of localised ageing of the cell and thus the premature ageing of battery packs. It will also facilitate a guideline for instrumentation and determining where to place thermal sensors, as well as giving information on the necessary cooling strategy. Improved temperature sensing methodology could underpin the development for more efficient battery thermal management systems, reducing computational complexity, weight and cost. In this paper, after outlining the experimental set up and procedure in Section 2, the results obtained are presented in Section 3 followed with a discussion in Section 4. Finally, the conclusions are summarised in Section 5.

2. Experimental Details

2.1 Cell Details

Two commercially available 20 Ah pouch cells were utilised in all the experiments. The cell has a LiC_6 negative electrode and lithium iron phosphate ($LiFePO_4$) positive electrode. The cell operates within a voltage window of 3.6 V (for charge) to 2.0 V (for discharge). The maximum continuous charge and discharge rate capabilities of the cell are defined on the manufacturer's datasheet as 3 and 10C, respectively. The cell dimensions are 7.25 x 160 x 227 mm.

2.2 Experimental Procedure

2.2.1 Discharge protocol

The first step of each experiment is to fully charged at 25°C the two cells. This was performed by discharging the cells to 2.0 V, followed by a four hour rest step, as it has been recently shown that this is the time required for lithium ion cell to settle electrochemically to an acceptable level [39]. Afterwards, the cells were charged using a constant current-constant voltage (CC-CV) method, applying 1C for the CC part to 3.6 V and then holding the voltage at 3.6 V for the CV part until the current drops to C/20. Within an hour of the full charge, the

chamber temperature was altered to the test temperature as shown in the test matrix in Table 1. After allowing the cells to soak at the test temperature for 4 hours, they were discharged to 2.0 V using the rates outlined in Table 1.

A temperature range of -10°C to 50°C is used for discharge and 0°C to 50°C for charge as per the manufacturer's datasheet. This is in line with the -20°C to 45°C operational range defined in [40] and similar to the operating range of -20 to 55 °C (discharge) and 0 to 45 °C (charge) typically quoted by battery manufacturers for the majority of current automotive lithium ion batteries [41].

Table 1: Cell discharge (D) and charge (C) matrix with temperature and C rate

Temperature	**Cell discharge**				
	0.5C	**1C**	**3C**	**5C**	**10C**
-10 °C	D	D	D	D	D
0 °C	D & C	D & C	D & C	D	D
10 °C	D & C	D & C	D & C	D	D
20 °C	D & C	D & C	D & C	D	D
30 °C	D & C	D & C	D & C	D	D
40 °C	D & C	D & C	D & C	D	D
50 °C	D & C	D & C	D & C	D	D

2.2.2 Charge protocol

For each charge rate, test cells were discharged to 2.0 V at 25 °C and subsequently the ambient temperature was changed to the values listed in Table 1. Cells were then charged at that temperature applying the CC-CV method, using the C rates as listed in Table 1 for the CC part to 3.6 V. In the CV part, 3.6 V was kept constant until current dropped to 1A. In contrast to the discharge protocol, -10 °C and the 5C and 10C test conditions were avoided for the charge tests to maintain the test conditions within the manufacturer datasheet of the cell.

2.2.3 Instrumentation

During the experiments, the temperature of the cell surface was recorded at 16 different locations, which are shown in Figure 1. A thermocouple was placed on each of the positive and negative tabs. The remaining 14 thermocouples were placed with seven on each side of the cell in identical geometric positions. Therefore, thermocouple position 'F12' is exactly on the opposite side of the 'F3' thermocouple, and similarly thermocouple 'F14' is on the opposite side to thermocouple position 'F8'. In Figure 1, *T* represents the tab width, *W* represents the cell width, and *H* represents the cell height excluding the tabs. The thermocouples used were K-type with an accuracy of ± 0.5˚C and data logging was performed using multiple Pico TC-08 data loggers at a one second sampling rate.

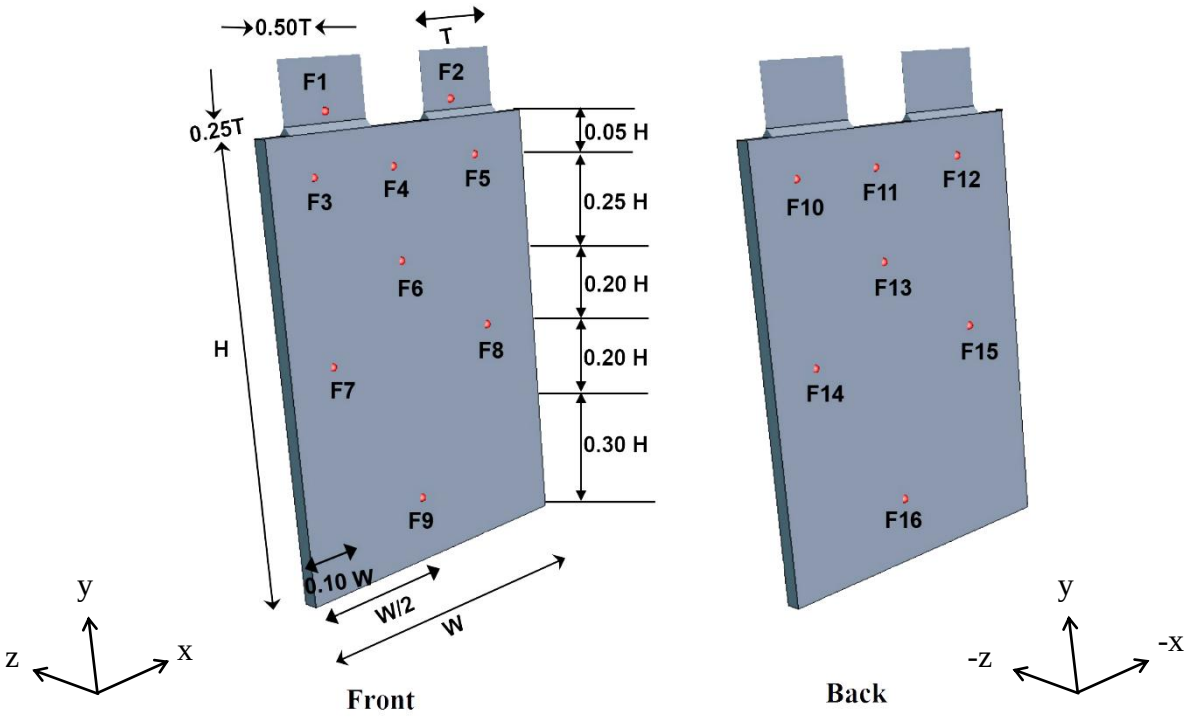

Figure 1: Thermocouple positions on the cell surface

2.3 Experimental Setup

Usually pouch cells are laid on a surface to make a stable connection with the test equipment. However, by doing so both surfaces of the cell would not have the same environment to dissipate heat since one surface is in contact with the test bed and the other surface is in contact with ambient air. In order to avoid this undesirable scenario, both cells were hung by their tabs as shown in Figure 2 (a). This method ensured that both cell surfaces had the same thermal medium and boundary conditions.

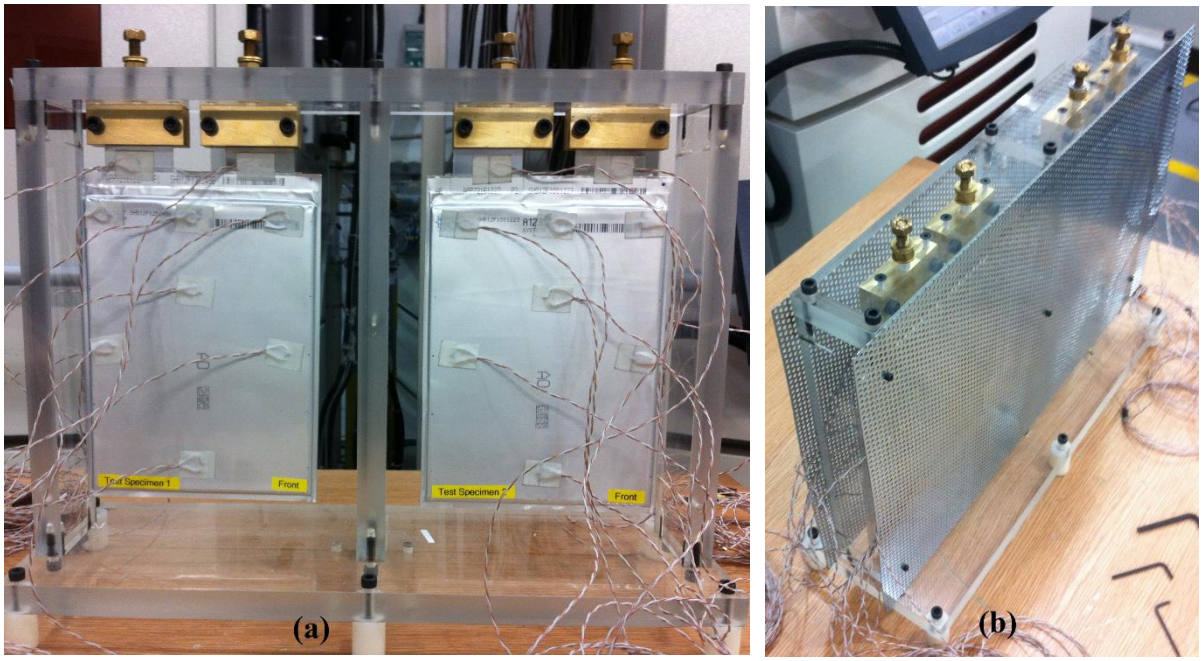

Figure 2: Cell connection with (a) test rig, (b) test rig is covered with a mesh.

The charge-discharge procedures were performed using a commercial cell cycler, namely Bitrode MCV 16-100-5. The test rig with cells as shown in Figure 2 (a) was placed within a thermal chamber (Weiss Gallenkamp Votsch VC^3 4060). Within the thermal chamber, heat is transferred through convection. In order to increase the heat transfer, air is circulated by an electric fan. This also reduces thermal gradients within the chamber. However, it was observed that depending on the relative location of the fan with respect to the cells, different air flow across the opposite sides of the cells and ultimately different cooling rates. In order to mitigate this undesirable phenomenon, a metallic mesh was applied on both side of the cells as shown in Figure 2 (b). The mesh was 5 cm away from cell surface on each side. The mesh creates air pockets which protects the cell surface from forced air flow but allows air to pass through at a slower rate, reducing the effect of convective cooling on the cell.

2.4 Error Analysis

Unless otherwise stated, the results are an average of both cells with error bars representing standard error (SE), defined as

$$SE = \frac{\sigma}{\sqrt{n}} \tag{1}$$

where σ is the standard deviation and n is the population size.

3. Experimental Results

3.1 Discharge

The average peak temperature rise for all 16 thermocouples at different ambient temperatures and discharge C rates for one cell is shown in Table 2. A two tailed homoscedastic student t-test with 5% significance level reveals that there is no statistically significant difference between the average peak temperatures of both cells.

Table 2: Average peak temperature rise (˚C ± SE) for discharge

Cell 1		C rate				
		0.5	1	3	5	10
Temperature (°C)	-10	7.4 ± 0.3	12.8 ± 0.5	25.9 ± 1.1	33.8 ± 1.4	47.1 ± 1.7
	0	6.6 ± 0.3	10.8 ± 0.5	21.9 ± 1.0	28.7 ± 1.2	41.2 ± 1.4
	10	4.9 ± 0.2	8.6 ± 0.4	18.3 ± 0.8	24.6 ± 1.0	35.2 ± 1.2
	20	3.6 ± 0.1	7.2 ± 0.3	14.8 ± 0.6	21.3 ± 0.7	31.3 ± 0.8
	30	1.9 ± 0.1	4.1 ± 0.2	10.9 ± 0.4	16.0 ± 0.5	25.9 ± 0.7
	40	1.0 ± 0.0	2.1 ± 0.1	7.1 ± 0.2	11.8 ± 0.3	22.0 ± 0.6
	50	1.1 ± 0.0	1.7 ± 0.1	5.5 ± 0.2	9.6 ± 0.2	19.3 ± 0.6

Table 2 shows that the cell surface temperature increase differs widely across the test matrix (see Table 1). At -10°C ambient temperature with 10C discharge, where the cells heat up by up 47.1-48.2°C while it is only 7.4-7.6°C with 0.5C discharge. A correlation between C rate and temperature rise is also observed at all the remaining ambient temperatures (0-50°C). This is in agreement with the literature [42–44], which occurs mainly because the Ohmic heating of lithium ion cells is proportional to the square of the current. Consequently, more heat is generated at the higher C rates.

A correlation between ambient temperature and the cell temperature rise can also be observed from Table 2, e.g. at 50 °C ambient temperature with 0.5C discharge, the cells only heat up by 1-1.1°C, whereas a 7.4-7.6°C °C temperature increase can be observed at -10 °C ambient for the same rate of discharge. Similarly, at 10C discharge, the cell temperature rises by 19.3-19.7 °C and 47-48 °C for the tests at 50°C and -10°C ambient respectively. This relationship is linear as shown in Figure 5(b), which is in agreement with the literature [33].

There are two fundamental mechanisms responsible for the relationship between cell temperature rise and ambient temperature. The first is that lithium ion cell Ohmic heating is proportional to the cell's internal resistance, which varies with cell temperature. The internal resistance of lithium ion cells increases at lower temperatures, and conversely, the resistance decreases at higher temperatures [45–47]. As a result, more heat is generated at the lower ambient temperatures. The second is that using a higher C rate will result in the cell discharging faster, and thus heat is generated for a shorter amount of time. This reduces the time during which heat can be dissipated to the environment and results in a higher temperature rise.

The colour coded peak temperature for each measurement point at different ambient temperatures (rows) and discharge C rates (columns) is shown in Figure 3. The first row of each table corresponds to the thermocouple number as described in Figure 1. For each ambient condition, the 16 surface temperatures (one for each thermocouple) are shown in ˚C and are formatted with 35 graduated colour scales, i.e. one for each temperature and C rate pair-wise combination. Blue indicates the coldest thermocouple locations and red indicates the hottest thermocouple locations. The darker the colour, the hotter/colder the point is. For example, at 0˚C ambient temperature and 1C discharge, the coldest location (blue) is thermocouple 2 at 6.7˚C and conversely, the hottest location (red) is thermocouple 6 at 12.9˚C. This allows us to visualise where the hot/cold spots are situated on the surface of the cell across the whole experimental matrix. Only one cell is shown for clarity as both cells behaved consistently during the experiments, both in terms of the absolute temperature as well as their distribution across the surface of the cell.

The colour coded scale displayed in Figure 3 shows that for most conditions (ambient temperature and C rate) the centre of the cell (thermocouple 6 and 13) is generally the hottest location (red) and the tabs (thermocouple 1 and 2) are the coldest (blue). This in agreement with the literature for NMC pouch cells [32, 33], however hotspots in the positive tab have been reported in LMO pouch cells [34]. These results are discussed in more detail in Section 4.1.

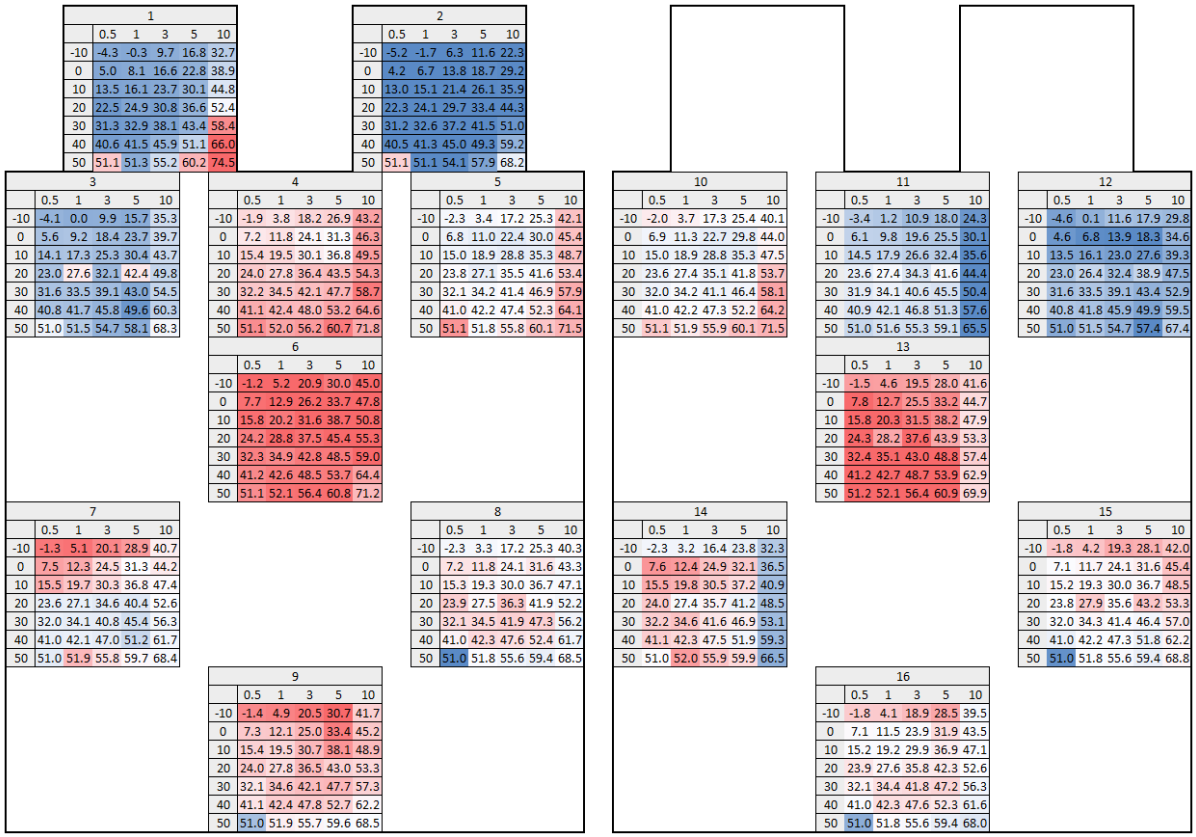

Figure 3: Maximum surface (*X*-*Y*) temperatures for different discharge C-rates (0.5-10C) and ambient conditions (–10˚C to 50˚C). Left: front, right: back of cell. Colour coded as dark blue representing the coldest and dark red representing the hottest thermocouple locations.

3.2 Charge

The colour coded temperature rise for each of the measurement at different ambient temperatures and charge C rates is shown in Figure 4. For each ambient condition, the 16 temperatures (one for each thermocouples) are shown in ˚C and are formatted with a two colour scale: dark blue for the coldest and dark red for the hottest location.

The colour coded scale presented in Figure 4 shows that for most conditions (ambient temperature and C rate) the centre of the cell is also generally the hottest location (red) and the tabs are the coldest (blue). The temperature distribution in Figure 4 (charge) is similar to the results for discharge shown in Figure 3, however the amplitude is smaller. These results are discussed in more detail in Section 4.2.1.

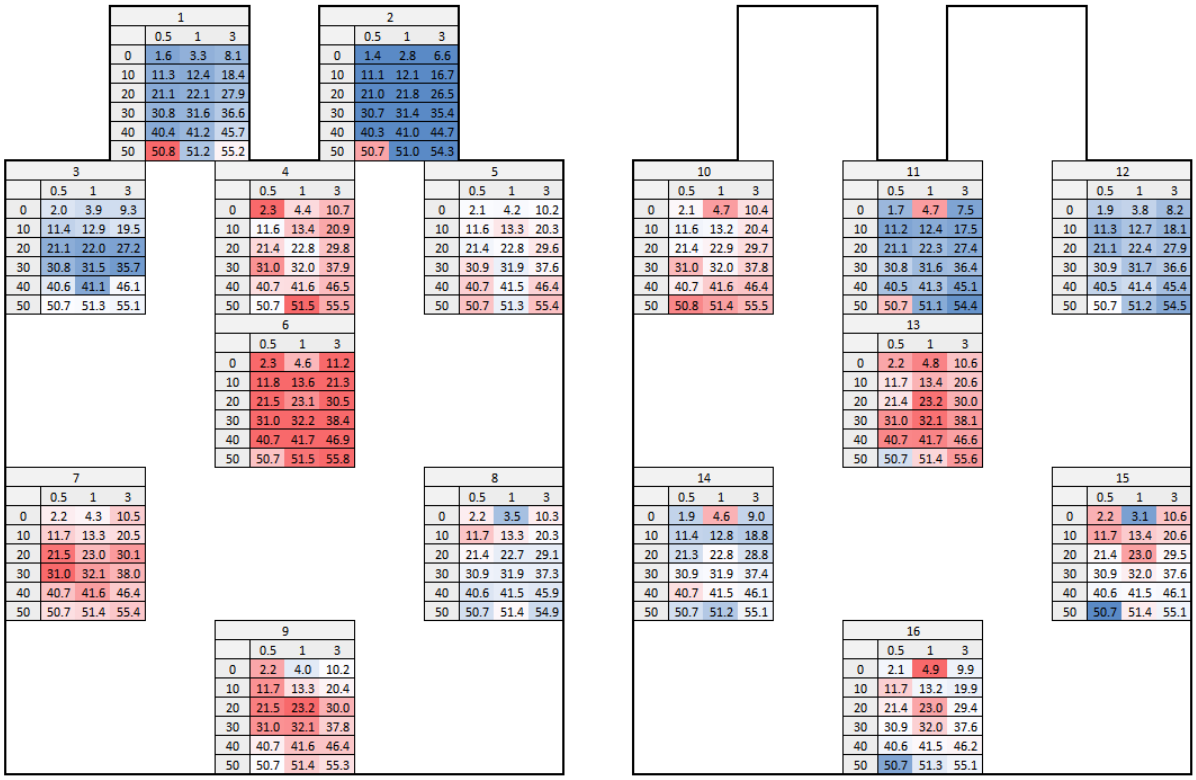

Figure 4: Maximum surface (*X*-*Y*) temperatures for different charge C-rates (0.5-3C) and ambient conditions (0˚C-50˚C). Left: front, right: back of cell. Colour coded as dark blue representing the coldest and dark red representing the hottest thermocouple locations.

3.3 Capacity

In lithium ion cells, the overpotential is the potential difference between the open circuit voltage and the terminal voltage observed during operation [48]. This voltage drop is a function of numerous battery parameters, including C rate: generally, increasing the C rate causes a higher overpotential. A consequence of a larger voltage drop is that the lower cut off voltage (2V for the cells utilised in this study) is reached sooner during a discharge and therefore less energy is extracted out of the cell. This yields an apparent capacity reduction with increasing C rates. The average capacity for both cells is plotted against C rate and ambient temperature in Figure 5(a), which shows that at the lower ambient temperatures, the capacity increases with C rate. This phenomenon is due to self-heating and is explained further in Section 4.3.

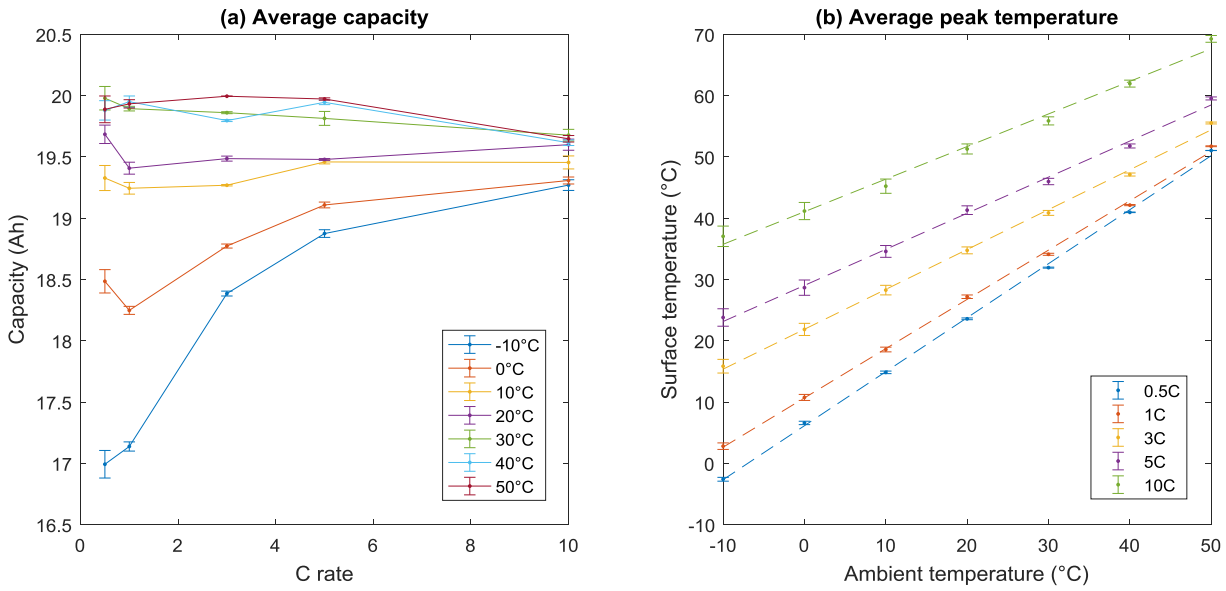

Figure 5: (a) Average capacity vs C rate, (b) Average cell surface peak temperature vs ambient temperature (Error bars represent ±SE)

4. Discussion

Since hotspots in the positive tabs are expected in LMO pouch cells [34], the discussion begins by addressing the phenomenon behind why the tabs are cooler in the results presented (see Figure 3-4). The main findings on the temperature gradients are discussed in Section 4.2.

4.1 Tab temperature explanation

From Figure 3-4, it can be seen that the aluminium positive tab (thermocouple 1) is generally hotter than the nickel plated copper negative tab (thermocouple 2). This is consistent with the literature for LMO cells [34] and is an intuitive result since aluminium has a higher resistivity (2.65×10^{-8} Ωm) than copper (1.68×10^{-8} Ωm) and the positive current collector is thicker than the negative current collector, e.g. 2mm and 1.4mm thickness for the Al and Cu foil respectively [49]. Figure 3 shows that the cell tabs are the coldest points of the cells, apart from 30-50°C at 10C discharge and 0.5C charge at 50°C for both cells. Whilst this is common in NMC cells [32, 33], LFP are expected to have hotpots at the tabs as reported for LMO cells [34]. A thermal model was developed in COMSOL Multiphysics software to investigate the phenomenon. A full description of the mathematical model, including the underpinning objectives, boundary conditions and parameterisation can be found in [50] and will therefore not be repeated here. The model was refined by modifying the effective

convective heat transfer coefficient on the edge of the cell as reported in [51]. Simulation revealed that the large brass connectors at the cell tabs and current carrying cables from battery cyclers are acting as heat sinks, drawing heat away from the tabs via conduction and dissipating it to ambient air via convection. It is assumed the cells are made up of electrode pairs, which are connected in parallel by the current collectors, and the collective behaviour of these pairs represents the overall cell thermal behaviour. Each electrode pair is modelled as a five layers, namely a negative current collector, a negative electrode, a separator, a positive electrode and a positive current collector. A 1D electrochemical-thermal model is used to calculate the cell self-heating, which is combined with a 3D thermal model in order to capture the temperature distribution of the cell and the brass blocks. A simulation of the surface temperature at the end of 5C discharge at 20˚C and 30˚C ambient temperature in shown in Figure 6. Table 3 confirms that the modelled temperatures correlate with the experimental values.

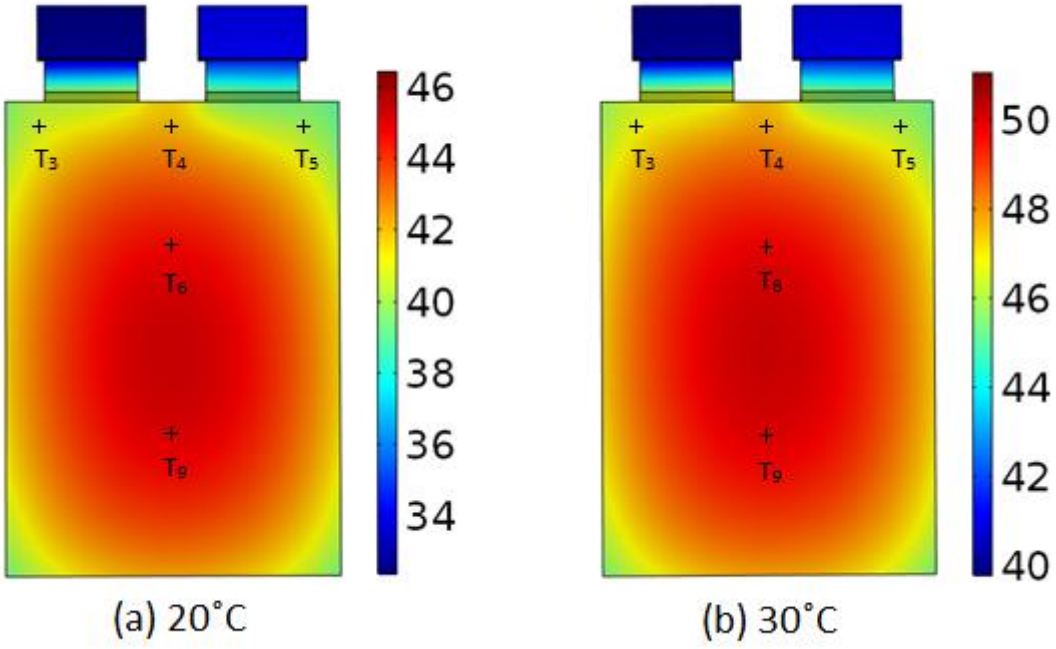

Figure 6: Thermal model temperature distribution at the end of 5C discharge at (a) 20˚C and (b) 30˚C ambient temperature (colour scale in ˚C)

Figure 6 confirms that heat dissipation from the brass blocks causes the tabs to be colder than the cell surface. It also corroborates that the centre of the cell (thermocouples 6 and 13) is the hottest point for this experimental set up.

Table 3: Measured and thermal model temperature at the end of 5C discharge

	20˚C Ambient		30˚C Ambient	
Thermocouple Location	Experimental (°C)	Model (°C)	Experimental (°C)	Model (°C)
T_3	42.4	41.2	43.0	47.2
T_4	43.5	42.1	47.7	47.8
T_5	41.6	40.5	46.9	46.5
T_6	45.4	44.6	48.5	49.7
T_9	43.0	43.0	47.7	48.4

However, at 10 C discharge and above 30˚C ambient temperature, the positive tab becomes the hottest point from (see Figure 3). This is because the heat generated in the tabs is proportional to the resistance of the tab and the square of the current applied. The temperature coefficient of resistance of aluminium and copper are 0.00429 and 0.00393 ppm/˚C, respectively [52]. Hence the positive and negative cell tabs will have 26% and 24% higher resistance at 50˚C compared to -10˚C, respectively. In contrast, the cell's resistance increases four fold at -10˚C compared to 50˚C. Consequently, proportionally less heat is generated in the cell than in the tabs at higher temperatures compared to lower temperatures. This is accentuated at the highest C rate (10C) since heat generation is proportional to the square of the current applied. At this C rate and elevated ambient, the positive tab becomes the hottest point.

Figure 6 shows the middle of the cell (thermocouples 6 and 13) is the hottest location (red) across all temperatures and C rates, excluding the cell tabs. At higher C rates, heat can be seen shifting from the bottom left of the cell (thermocouples 7 and 9) towards the top (thermocouple 4) and top right (thermocouple 5) of the cell. This effect can be explained by the current density within the cell which is directly related to the cell's internal architecture. Lithium ion pouch cells are constructed in multiple layers of sandwiched electrodes, current collectors and separator [53]. Current collectors from each layer of the positive and negative electrodes are welded together with the cell tabs to make the external connection. Therefore, within the current collector, current flows towards the top of the cell and current density increases towards the top of the cell. Heat generation and temperature rise naturally follows the current density.

4.2 Temperature gradients

The temperature gradients on both sides of the cell follow a similar pattern with the exception of the middle top where thermocouples 4 and 11 were placed. The gradient between the two sides at this point reaches 18.9°C at -10°C ambient temperature with 10C discharge. This might be associated with the tab position across the thickness of the battery cell. Ideally, the cell tab would be placed exactly in the middle of the thickness of the battery. However, as is the case for the cell tested as part of this study, it is a common practice in lithium ion cell manufacturing to place the tab close to one of the cell surfaces. The tabs are placed close to the front surface, i.e. where thermocouples 1-9 are, and therefore the current density close to this surface is expected to be higher. As a consequence, thermocouples 3, 4 and 5 are expected to record a higher temperature than thermocouples 10, 11 and 12; as reflected in the temperature gradient observed. The highest gradient occurs at the middle (thermocouple 4), because it is affected by both the positive and negative tabs. This effect has not been reported in the literature previously; other studies on thermal gradients in large pouch cells [32–34] could only consider temperature gradients on one surface.

Large temperature gradients, defined as the cell surface temperature range (i.e. maximum temperature minus minimum temperature - excluding tabs), were observed on both cells, up to 20.7 °C at -10 °C ambient temperature with 10C discharge. Figure 7 shows the temperature gradients (average of both cells) in both directions, i.e. in plane with the stack (across the cell surface) and perpendicular to the stack (across the thickness of the cell). The temperature gradients in both planes have similar behaviour: they decrease with increasing ambient temperature, and increase with increasing C rates. This is consistent with heat generation: the more heat generated, the higher the gradient.

Figure 7 shows the gradients have similar magnitude; on average the in-plane gradient was found to be 1.1 ± 0.2°C larger than the thermal gradients perpendicular to the stack. Whilst lithium ion cells are known to exhibit anisotropic thermal conductivity; e.g. 24.9 $Wm^{-1}K^{-1}$ in the *X* and *Y* directions compared to 1.04 $Wm^{-1}K^{-1}$ in the *Z* direction [49], the width (*X* = 160 mm) and cell length (*Y* = 227mm) and are 22 and 31 times larger than the thickness (*Z* = 7.25mm) respectively, therefore similar gradient are expected.

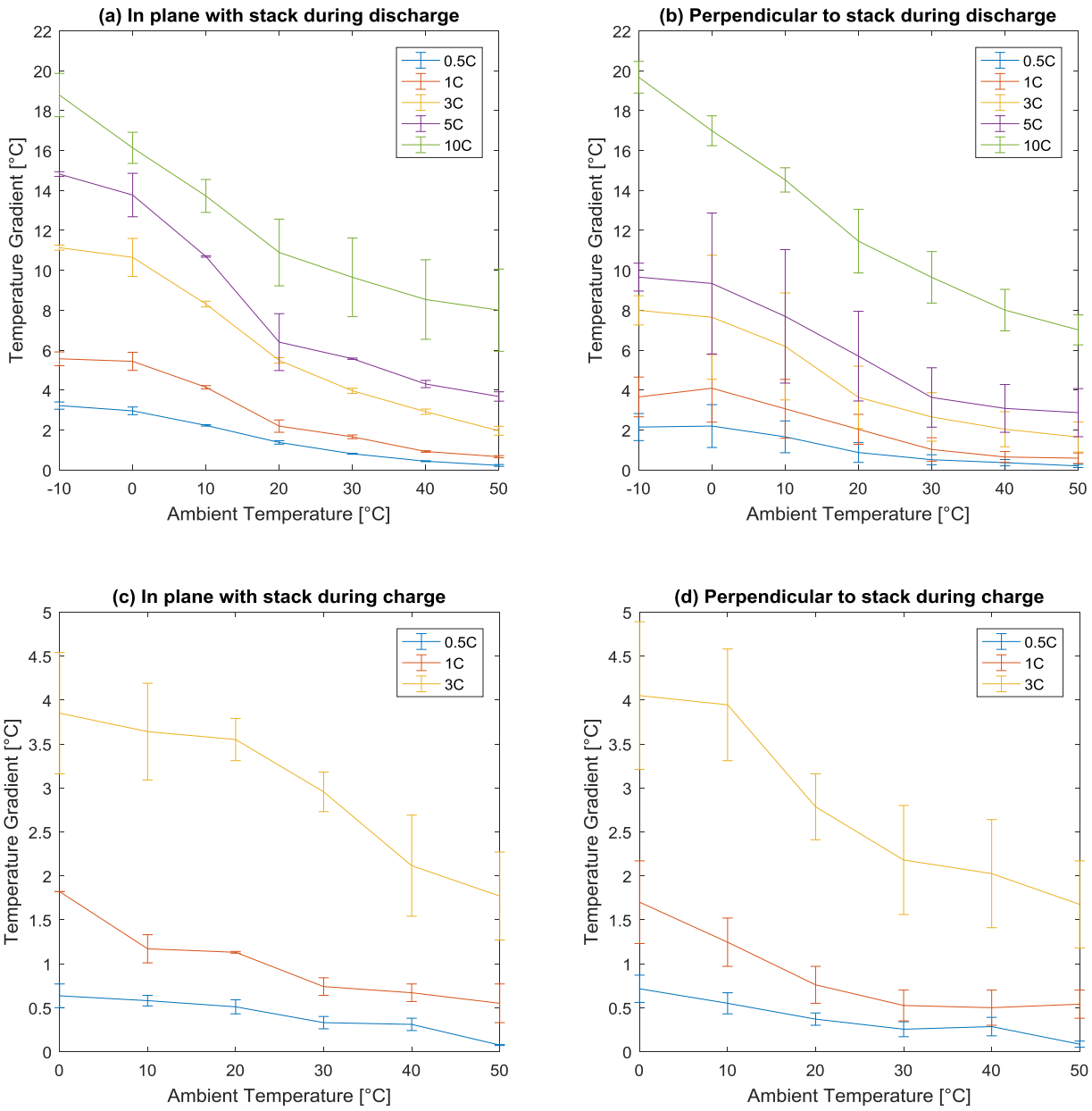

Figure 7: Average maximum cell temperature gradient (excluding tabs) for different C-rates and ambient conditions (Error bars represent ± SE)

As a consequence of thermal gradients, current density and SoC inhomogeneities occur within the cell, which cause localised ageing [29] and reduce the efficiency and lifespan of the battery. To reduce localised ageing, original equipment manufacturer (OEMs) aim to achieve 3-5°C temperature gradient within the battery pack. The gradients shown in Figure 7 reveal that at minus 10°C ambient temperature, only 0.5C would keep this cell within the target gradient. At 20°C ambient temperature, only 1C meets the target gradient requirement. These C-rates are prohibitive for automotive applications and improved cooling is therefore

required. Whilst this result has been shown in 20Ah LFP cells, the authors speculate that this phenomenon would apply to most large pouch cells, regardless of chemistry. Temperature gradient across the cell thickness are also expected to increase for thicker cells.

Since pouch cells are thin, it has wrongly been assumed that the thermal gradient across the thickness of the cell is small and therefore can be ignored. Figure 7 highlights that significant thermal gradients perpendicular to the stack layers are present at low temperature and high C-rates. It has been shown that temperature gradients perpendicular to the stack layers may lead to higher local currents and faster degradation compared to temperature gradients in-plane with the stack layers; for example, a 5Ah NCM cathode pouch cells was tested for 1,000 cycles and surface cooling resulted in a loss of usable capacity three times higher than cell tab cooling [26]. This effect is likely to be accentuated in larger pouch cells, where we have shown larger thermal gradients are present for high C rate applications such as in the automotive industry [54].

Ideally, battery pack designers need to place a thermal sensor at the hottest and coldest points in order to monitor the temperature gradient across the cell. However, monitoring temperature gradients within battery packs is challenging, as there are limitations on the number of sensors that can be placed within a pack, due to cost and weight constraints. Since the thermal gradient perpendicular to the stack has been shown to be up to three times more detrimental with regard to cell ageing, the authors assert that it is crucial for lithium ion pack manufacturers to consider the temperature on both sides of the cells utilised. This type of study can be used to calculate the cooling requirements of the thermal management system in order to maintain the cells within the desired temperature. Assuming a thermal capacity of 500 Joules per Kelvin, the cooling system would be required to extract 7500 Joules of heat in order to maintain the cell within 5°C during a full 10C discharge at -10°C ambient. In addition, this study suggests that the cooling system needs to extract more heat from the top of the cell compared to the bottom of the cell. Therefore, this could be adapted to assist in the development of a more efficient cooling strategy.

4.2.1 Charge

Although Ohmic heating of an electrical system is independent of the direction of current, lithium ion batteries are not pure Ohmic devices; they are complex electrochemical devices that exhibit capacitive and inductive behaviour. The complex impedance changes with

direction of current as intercalation and de-intercalation of lithium ion within the electrode is reversed. As a result, lithium ion batteries perform differently during charge and discharge; typically, lithium ion battery internal resistance can be 5-20% higher during charge [55]. However, this does not translate to higher temperature rises during charge since a CCCV charging protocol is implemented. Consequently, the charge takes longer, since some of the charge is performed at a lower current whilst maintaining the voltage constant. For example, a 3C discharge at 20˚C ambient takes 20 minutes, whilst a 3C charge takes around 53 minutes. The peak in temperature during charge occurs at the end of the CC part. As a result, the temperature rise is smaller during charge (Figure 4) compared to discharge (Figure 3).

Figure 4 confirms that the temperature gradient and hotspots are similar during charge and discharge. The temperature gradient observed across the thickness of the cell during discharge, i.e. thermocouple 4 vs 11, follow a similar pattern during charge, suggesting that the current densities are distributed identically during both charge and discharge, which has not been reported previously as the majority of studies only consider discharging.

Figure 7 (c) and (d) confirm that the temperature gradients in-plane have similar magnitude to the gradients perpendicular to the stack.

4.3 Self-heating effect

As mentioned in Section 3.3, the cell capacity increased with C rate at low ambient temperature. Cell voltage vs capacity curves at -10 °C ambient for five different C-rates (0.5 – 10C) are plotted in Figure 8(a) to investigate this result. It can be seen from this figure that the cell voltage increases during the discharge at the higher C rates (1C and above).

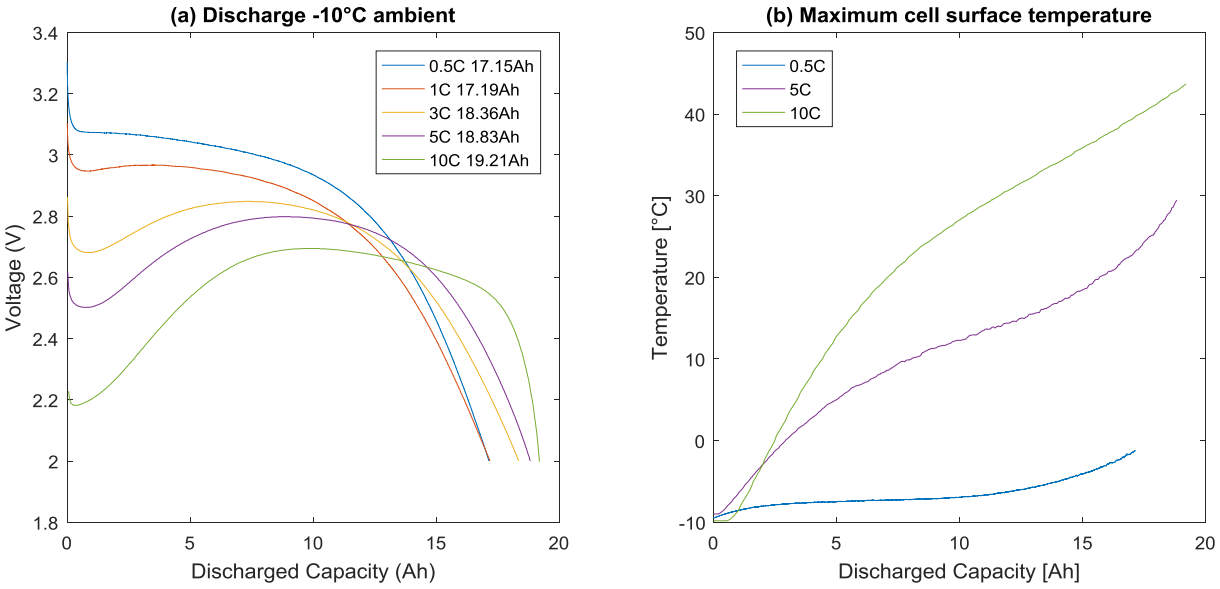

Figure 8: (a) Cell voltage vs capacity at -10°C ambient, (b) Maximum temperature on cell surface during discharge test at -10°C ambient

When a cell is fully discharged, i.e. from 100 % to 0 % SoC, the cell voltage can be split into three sections [53, 56]. In the first part, at the beginning of the discharge there is a sharp drop in voltage, which increases with discharge rate, e.g. approximately 200mV for 0.5C test, whereas it is 1.0 V for 10C rate (see Figure 8(a)). This drop is mainly due to the pure Ohmic resistance and faradic charge transfer resistance of the cell [53, 56]. The next section of discharge is a relatively flat region where the voltage drops slowly with respect to capacity. This is due to a gradual impedance increase because of changes in the lithium surface concentration of the active material [53, 56]. The electromotive force of the lithium ion battery is altered and diffusion slows down since fewer lithium ions are available to translocate into the active material [53, 56]. In the third and final part, towards the end of discharge, there is a sharp drop in voltage to the minimum cell voltage. The voltage changes rapidly due to severe cell polarisation caused by depletion of active materials in the electrode regions. Cell reactants near the electrodes have been consumed and diffusion of additional reactants from the bulk is too slow [56]. This effect is accentuated at high temperatures, since it results in faster consumption of the cell reactants causing a larger increase in polarisation resistance at the end of the discharge, and consequently, a greater drop in voltage [57].

However, Figure 8(a) shows that the voltage behaviour is different at higher C rates due to self-heating of the cell, which is accentuated at the low temperature (-10°C) shown here. The temperature rise on the cell surface during 5C and 10C discharges at -10 °C is shown in

Figure 8(b). It can be seen that there is a steep temperature rise up to 8 Ah discharge, which is directly associated with the voltage rise shown in Figure 8(a). In contrast, at 0.5 C rate this behaviour is not present as the temperature rise is much lower. As discussed previously, the organic electrolyte used in lithium ion batteries makes the internal resistance more temperature dependent than other types of batteries [23]. Self heating during discharge increases the ion transport properties of the electrolyte [58]. The electrolyte becomes less viscous with increasing temperature, effectively increasing the mobility of the ions [57], which decreases the oveall internal resistance of the cell. Due to this decrease of internal resistance, the overpotential decreases, and thus, the cell voltage increases and more capacity can be extracted, as shown in Figure 8(a). The self heating effect raises the cell temperature so significantly that 13.4 ± 0.7% capacity can be extracted using a 10C discharge compared to a 0.5C discharge at -10°C ambient temperature.

At lower temperatures, the cell internal resistance is higher resulting in higher Ohmic heating, which means that the effect is more noticeable. From Figure 3, it can be seen that the maximum temperature increase is almost double the lowest temperature: at 50˚C ambient, the hottest point reaches 74.5˚C, i.e. a 24.5˚C temperature increase, whereas at –10˚C, the hottest point reaches 45˚C, i.e. a 55˚C temperature increase. Ohmic heating is also proportional to the square of current and therefore there is more heat generated at the higher C-rates and the self heating effect is more pronouced and the highest capacity values are obtained as shown in Figure 8.

Based on these results, it might be acceptable or indeed preferable for the battery to discharge with higher current at lower temperature to warm up. However, the use of excessive high current especially at lower temperature accelerates ageing [15, 59, 60] and also poses a potential safety risk [53]. Therefore, it is important to find a balance between these two contrasting mechanisms.

4.4 Further work

The results highlight that large temperature gradients develop within 20 Ah LFP pouch cells at low ambient temperatures and C rates, which may lead to adverse voltage distributions and differential ageing within the cell. Broadening the experimental programme to include cells from a cross section of manufacturers, formats and chemistries will further highlight the transferability of these results to other cell technologies. Based on these results, the authors

are currently investigating a range of areas for further work. The first is focussed on instrumenting cells with temperature sensors embedded within the cell layers. This will allow internal cell temperature within the stack to be monitored and thermal gradient between layers to be investigated. The second area of further work aims to incorporate forced cooling schemes within the experimental set-up in order to evaluate the impact of cooling strategies on cell thermal gradients. The third area of further aims to quantify the long-term impact of high C rates on cell degradation and lifetime.

5. Conclusion

In this study the temperature on both sides of a large pouch cell has been investigated for a wide range of ambient temperatures (-10°C to 50°C) and C rates (0.5C to 10C). The experimental setup and thermocouple placement used allowed for temperature gradients across the cell surface (in line with the stack) and across the cell thickness (perpendicular to the stack) to be investigated for both charge and discharge, which has not been reported in the literature previously; since other studies on thermal gradients on large pouch cells only consider one surface. It was shown that the temperature gradients were found to increase with increasing C rate and decreasing temperature. At the highest C rate (10C) and lowest ambient temperature (-10°C), the in plane gradient reached 18.8˚C and the thermal gradient perpendicular to the stack was 19.7˚C, which is much higher than previously reported in the literature. A thermal distribution model across the cell surface was developed which agrees with the experimental results reported here. It was identified that the top of the cell, close to the tabs, are not the hottest area, as commonly referred in literature. The metallic bus-bars with high thermal conductivity connected with the cell tabs were identified providing a faster cooling medium.

The gradients result in large current density distributions and local state of charge differences within the cell and battery pack, leading to premature ageing. The temperature gradients measured are much higher than the current industry maximum 5˚C thermal gradient across the entire pack used in the automotive industry to minimise localise ageing.

Acknowledgements

The research presented within this paper is supported by the Innovate UK (https://hvm.catapult.org.uk/) through the WMG centre High Value Manufacturing (HVM)

Catapult in collaboration with Jaguar Land Rover and TATA Motors. The authors are thankful to all ‘cell work-stream’ members of HVM Catapult for their valuable advice, comments and discussions.

References

[1] The European Parliament and the Council of the European Union, 'Regulation (EU) No 333/2014 of the European Parliament and of the Council of 11 March 2014 Amending Regulation (EC) No 443/2009 to Define the Modalities for Reaching the 2020 Target to Reduce CO2 Emissions From New Passenger Cars', *Off. J. Eur. Union*, vol. L103, pp. 15–21, 2014.

[2] J. H. Seinfeld and S. N. Pandis, *Atmospheric chemistry and physics : from air pollution to climate change*. Hoboken, NJ, USA: John Wiley & Sons, 2016.

[3] K. G. Høyer, 'The history of alternative fuels in transportation: The case of electric and hybrid cars', *Util. Policy*, vol. 16, no. 2, pp. 63–71, 2008.

[4] H. Lund and W. W. Clark Ii, 'Sustainable energy and transportation systems introduction and overview', *Sustain. Energy Transp. Syst*, vol. 16, pp. 59–62, 2008.

[5] United States Department of Energy, 'One Million Electric Vehicles By 2015 Status Report Executive Summary', 2015.

[6] K. E. Aifantis, S. A. Hackney, R. V. Kumar, and Wiley InterScience (Online service), *High energy density lithium batteries : materials, engineering, applications*. Hoboken, NJ, USA: John Wiley & Sons, 2010, 2010.

[7] D. Andre, M. Meiler, K. Steiner, C. Wimmer, T. Soczka-Guth, and D. U. Sauer, 'Characterization of high-power lithium-ion batteries by electrochemical impedance spectroscopy. I. Experimental investigation', *J. Power Sources*, vol. 196, no. 12, pp. 5334–5341, 2011.

[8] H.-M. Cho, W.-S. Choi, J.-Y. Go, S.-E. Bae, and H.-C. Shin, 'A study on time-dependent low temperature power performance of a lithium-ion battery', *J. Power Sources*, vol. 198, pp. 273–280, 2012.

[9] S. Rodrigues, N. Munichandraiah, and A. K. Shukla, 'AC impedance and state-of-charge analysis of a sealed lithium-ion rechargeable battery', *J. Solid State Electrochem.*, vol. 3, no. 7–8, pp. 397–405, Sep. 1999.

[10] Q. Wang, P. Ping, X. Zhao, G. Chu, J. Sun, and C. Chen, 'Thermal runaway caused

fire and explosion of lithium ion battery', *J. Power Sources*, vol. 208, pp. 210–224, 2012.

[11] S. Al Hallaj, H. Maleki, J. S. Hong, and J. R. Selman, 'Thermal modeling and design considerations of lithium-ion batteries', *J. Power Sources*, vol. 83, no. 1, pp. 1–8, 1999.

[12] D. P. Abraham, J. L. Knuth, D. W. Dees, I. Bloom, and J. P. Christophersen, 'Performance degradation of high-power lithium-ion cells—Electrochemistry of harvested electrodes', *J. Power Sources*, vol. 170, no. 2, pp. 465–475, 2007.

[13] M. Broussely *et al.*, 'Main aging mechanisms in Li ion batteries', *J. Power Sources*, vol. 146, no. 1, pp. 90–96, 2005.

[14] H. Yamada, Y. Watanabe, I. Moriguchi, and T. Kudo, 'Rate capability of lithium intercalation into nano-porous graphitized carbons', *Solid State Ionics*, vol. 179, no. 27, pp. 1706–1709, 2008.

[15] J. Vetter *et al.*, 'Ageing mechanisms in lithium-ion batteries', *J. Power Sources*, vol. 147, no. 1, pp. 269–281, 2005.

[16] B. Y. Liaw, E. P. Roth, R. G. Jungst, G. Nagasubramanian, H. L. Case, and D. H. Doughty, 'Correlation of Arrhenius behaviors in power and capacity fades with cell impedance and heat generation in cylindrical lithium-ion cells', *J. Power Sources*, vol. 119, pp. 874–886, 2003.

[17] S. Käbitz *et al.*, 'Cycle and calendar life study of a graphite|LiNi1/3Mn1/3Co1/3O2 Li-ion high energy system. Part A: Full cell characterization', *J. Power Sources*, vol. 239, pp. 572–583, 2013.

[18] M. Ecker *et al.*, 'Calendar and cycle life study of Li(NiMnCo)O2-based 18650 lithium-ion batteries', *J. Power Sources*, vol. 248, pp. 839–851, 2014.

[19] T. Waldmann, M. Wilka, M. Kasper, M. Fleischhammer, and M. Wohlfahrt-Mehrens, 'Temperature dependent ageing mechanisms in Lithium-ion batteries – A Post-Mortem study', *J. Power Sources*, vol. 262, pp. 129–135, 2014.

[20] H. Maleki, G. Deng, A. Anani, and J. Howard, 'Thermal Stability Studies of Li-Ion

Cells and Components', *J. Electrochem. Soc.*, vol. 146, no. 9, p. 3224, 1999.

[21] X. Zhang, 'Thermal analysis of a cylindrical lithium-ion battery', *Electrochim. Acta*, vol. 56, no. 3, pp. 1246–1255, 2011.

[22] T. Waldmann, S. Gorse, T. Samtleben, G. Schneider, V. Knoblauch, and M. Wohlfahrt-Mehrens, 'A Mechanical Aging Mechanism in Lithium-Ion Batteries', *J. Electrochem. Soc.*, vol. 161, no. 10, pp. A1742–A1747, Jul. 2014.

[23] T. M. Bandhauer, S. Garimella, and T. F. Fuller, 'A Critical Review of Thermal Issues in Lithium-Ion Batteries', *J. Electrochem. Soc.*, vol. 158, no. 3, p. R1, 2011.

[24] Padampat Chander Bhatia, 'THERMAL ANALYSIS OF LITHIUM-ION BATTERY PACKS AND THERMAL MANAGEMENT SOLUTIONS', The Ohio State University, 2013.

[25] G. Karimi and A. R. Dehghan, 'Thermal Management Analysis of a Lithium-Ion Battery Pack using Flow Network Approach', *Int. J. Mech. Eng. Mechatronics J.*, vol. 1, no. 1, 2012.

[26] I. A. Hunt, Y. Zhao, Y. Patel, and G. Offer, 'Surface Cooling Causes Accelerated Degradation Compared to Tab Cooling for Lithium-Ion Pouch Cells', *J. Electrochem. Soc.*, vol. 163, no. 9, pp. A1846–A1852, Jul. 2016.

[27] J. Cao and A. Emadi, 'Batteries Need Electronics', *IEEE Ind. Electron. Mag.*, vol. 5, no. 1, pp. 27–35, Mar. 2011.

[28] 'Nissan Leaf teardown (Part 1) - MarkLines Automotive Industry Portal', 2012. [Online]. Available: https://www.marklines.com/en/report_all/rep1049_201202#report_area_2. [Accessed: 11-Nov-2016].

[29] M. Fleckenstein, O. Bohlen, M. A. Roscher, and B. Bäker, 'Current density and state of charge inhomogeneities in Li-ion battery cells with LiFePO4 as cathode material due to temperature gradients', *J. Power Sources*, vol. 196, no. 10, pp. 4769–4778, 2011.

[30] T. Waldmann and M. Wohlfahrt-Mehrens, 'In-Operando Measurement of Temperature

Gradients in Cylindrical Lithium-Ion Cells during High-Current Discharge', *ECS Electrochem. Lett.*, vol. 4, no. 1, pp. A1–A3, Oct. 2014.

[31] S. Gorse *et al.*, 'An Explanation of the Ageing Mechanism of Li-Ion Batteries by Metallographic and Material Analysis', *Pract. Metallogr.*, vol. 51, no. 12, pp. 829–848, Dec. 2014.

[32] T. Waldmann *et al.*, 'Influence of Cell Design on Temperatures and Temperature Gradients in Lithium-Ion Cells: An In Operando Study', *J. Electrochem. Soc.*, vol. 162, no. 6, pp. A921–A927, Mar. 2015.

[33] C. Veth, D. Dragicevic, and C. Merten, 'Thermal characterizations of a large-format lithium ion cell focused on high current discharges', *J. Power Sources*, vol. 267, pp. 760–769, 2014.

[34] U. Seong Kim, J. Yi, C. B. Shin, T. Han, and S. Park, 'Modeling the Dependence of the Discharge Behavior of a Lithium-Ion Battery on the Environmental Temperature', *J. Electrochem. Soc.*, vol. 158, no. 5, p. A611, 2011.

[35] S. Goutam *et al.*, 'Surface temperature evolution and the location of maximum and average surface temperature of a lithium-ion pouch cell under variable load profiles', in *European Electric Vehicle Congress*, 2014.

[36] M. Xu, Z. Zhang, X. Wang, L. Jia, and L. Yang, 'Two-dimensional electrochemical–thermal coupled modeling of cylindrical LiFePO4 batteries', *J. Power Sources*, vol. 256, pp. 233–243, 2014.

[37] Y. Yin *et al.*, 'High-rate capability of LiFePO4 cathode materials containing Fe2P and trace carbon', *J. Power Sources*, vol. 199, pp. 256–262, 2012.

[38] Y. Wang *et al.*, 'A stable and high-capacity anode for lithium-ion battery: Fe2O3 wrapped by few layered graphene', *J. Power Sources*, vol. 288, pp. 314–319, 2015.

[39] A. Barai, G. H. Chouchelamane, Y. Guo, A. McGordon, and P. Jennings, 'A study on the impact of lithium-ion cell relaxation on electrochemical impedance spectroscopy', *J. Power Sources*, vol. 280, pp. 74–80, 2015.

[40] J. (John T. . Warner, *The handbook of lithium-ion battery pack design : chemistry,*

components, types and terminology, 1st ed. Elsevier, 2015.

[41] L. Lu, X. Han, J. Li, J. Hua, and M. Ouyang, 'A review on the key issues for lithium-ion battery management in electric vehicles', *J. Power Sources*, vol. 226, pp. 272–288, 2013.

[42] S. Chacko and Y. M. Chung, 'Thermal modelling of Li-ion polymer battery for electric vehicle drive cycles', *J. Power Sources*, vol. 213, pp. 296–303, 2012.

[43] Y. Ye, Y. Shi, N. Cai, J. Lee, and X. He, 'Electro-thermal modeling and experimental validation for lithium ion battery', *J. Power Sources*, vol. 199, pp. 227–238, 2012.

[44] K. Chen, G. Unsworth, and X. Li, 'Measurements of heat generation in prismatic Li-ion batteries', *J. Power Sources*, vol. 261, pp. 28–37, 2014.

[45] T. Momma, M. Matsunaga, D. Mukoyama, and T. Osaka, 'Ac impedance analysis of lithium ion battery under temperature control', *J. Power Sources*, vol. 216, pp. 304–307, 2012.

[46] L. H. J. Raijmakers, D. L. Danilov, J. P. M. van Lammeren, M. J. G. Lammers, and P. H. L. Notten, 'Sensorless battery temperature measurements based on electrochemical impedance spectroscopy', *J. Power Sources*, vol. 247, pp. 539–544, 2014.

[47] J. Zhang, H. Ge, Z. Li, and Z. Ding, 'Internal heating of lithium-ion batteries using alternating current based on the heat generation model in frequency domain', *J. Power Sources*, vol. 273, pp. 1030–1037, 2015.

[48] A. J. Bard and L. R. Faulkner, *Electrochemical methods : fundamentals and applications*. Wiley, 2001.

[49] S. C. Chen, C. C. Wan, and Y. Y. Wang, 'Thermal analysis of lithium-ion batteries', *J. Power Sources*, vol. 140, no. 1, pp. 111–124, 2005.

[50] D. Worwood *et al.*, 'Thermal analysis of lithium-ion pouch cells under aggressive automotive duty cycles with minimal cooling', in *IET Hybrid Electric Vehicle Conference*, 2016.

[51] U. S. Kim, C. B. Shin, and C.-S. Kim, 'Effect of electrode configuration on the thermal

behavior of a lithium-polymer battery', *J. Power Sources*, vol. 180, no. 2, pp. 909–916, 2008.

[52] D. Giancoli, *Physics: principles with applications*. Pearson Education, 2005.

[53] D. and T. B. R. Linden, *Handbook of Batteries*. McGraw-Hill, 2002.

[54] F. Krismer and J. W. Kolar, 'Accurate Power Loss Model Derivation of a High-Current Dual Active Bridge Converter for an Automotive Application', *IEEE Trans. Ind. Electron.*, vol. 57, no. 3, pp. 881–891, Mar. 2010.

[55] A. Barai, K. Uddin, W. D. Widanage, A. McGordon, and P. Jennings, 'Comparison of characterisation methodologies of internal impedance of lithium-ion cell and their interpretation', *Appl. Energy, Under Rev.*, 2016.

[56] J. Jiang and C. (Chemist) Zhang, *Fundamentals and applications of lithium-ion batteries in electric drive vehicles*. Wiley, 2015.

[57] B. Saha and K. Goebel, 'Modeling Li-ion Battery Capacity Depletion in a Particle Filtering Framework', in *Proceedings of the annual conference of the prognostics and health management society*, 2009, pp. 2909–2924.

[58] K. Smith and C.-Y. Wang, 'Power and thermal characterization of a lithium-ion battery pack for hybrid-electric vehicles', *J. Power Sources*, vol. 160, no. 1, pp. 662–673, 2006.

[59] X. Han, M. Ouyang, L. Lu, J. Li, Y. Zheng, and Z. Li, 'A comparative study of commercial lithium ion battery cycle life in electrical vehicle: Aging mechanism identification', *J. Power Sources*, vol. 251, pp. 38–54, 2014.

[60] M. Petzl, M. Kasper, and M. A. Danzer, 'Lithium plating in a commercial lithium-ion battery – A low-temperature aging study', *J. Power Sources*, vol. 275, pp. 799–807, 2015.

Table 1

Table 1: Cell discharge (D) and charge (C) matrix with temperature and C rate

Temperature	**Cell discharge**				
	0.5C	**1C**	**3C**	**5C**	**10C**
-10 °C	D	D	D	D	D
0 °C	D & C	D & C	D & C	D	D
10 °C	D & C	D & C	D & C	D	D
20 °C	D & C	D & C	D & C	D	D
30 °C	D & C	D & C	D & C	D	D
40 °C	D & C	D & C	D & C	D	D
50 °C	D & C	D & C	D & C	D	D

Table 2

Table 1: Average peak temperature rise (˚C ± SE) for discharge

Cell 1		C rate				
		0.5	1	3	5	10
Temperature (°C)	-10	7.4 ± 0.3	12.8 ± 0.5	25.9 ± 1.1	33.8 ± 1.4	47.1 ± 1.7
	0	6.6 ± 0.3	10.8 ± 0.5	21.9 ± 1.0	28.7 ± 1.2	41.2 ± 1.4
	10	4.9 ± 0.2	8.6 ± 0.4	18.3 ± 0.8	24.6 ± 1.0	35.2 ± 1.2
	20	3.6 ± 0.1	7.2 ± 0.3	14.8 ± 0.6	21.3 ± 0.7	31.3 ± 0.8
	30	1.9 ± 0.1	4.1 ± 0.2	10.9 ± 0.4	16.0 ± 0.5	25.9 ± 0.7
	40	1.0 ± 0.0	2.1 ± 0.1	7.1 ± 0.2	11.8 ± 0.3	22.0 ± 0.6
	50	1.1 ± 0.0	1.7 ± 0.1	5.5 ± 0.2	9.6 ± 0.2	19.3 ± 0.6

Table 3

Table 1: Measured and thermal model temperature at the end of 5C discharge

	20˚C Ambient		30˚C Ambient	
Thermocouple Location	Experimental (°C)	Model (°C)	Experimental (°C)	Model (°C)
T_3	42.4	41.2	43.0	47.2
T_4	43.5	42.1	47.7	47.8
T_5	41.6	40.5	46.9	46.5
T_6	45.4	44.6	48.5	49.7
T_9	43.0	43.0	47.7	48.4

Figure 1

Click here to download Figure(s) - provide separately in addition to within the manuscript file: Figure 1.docx

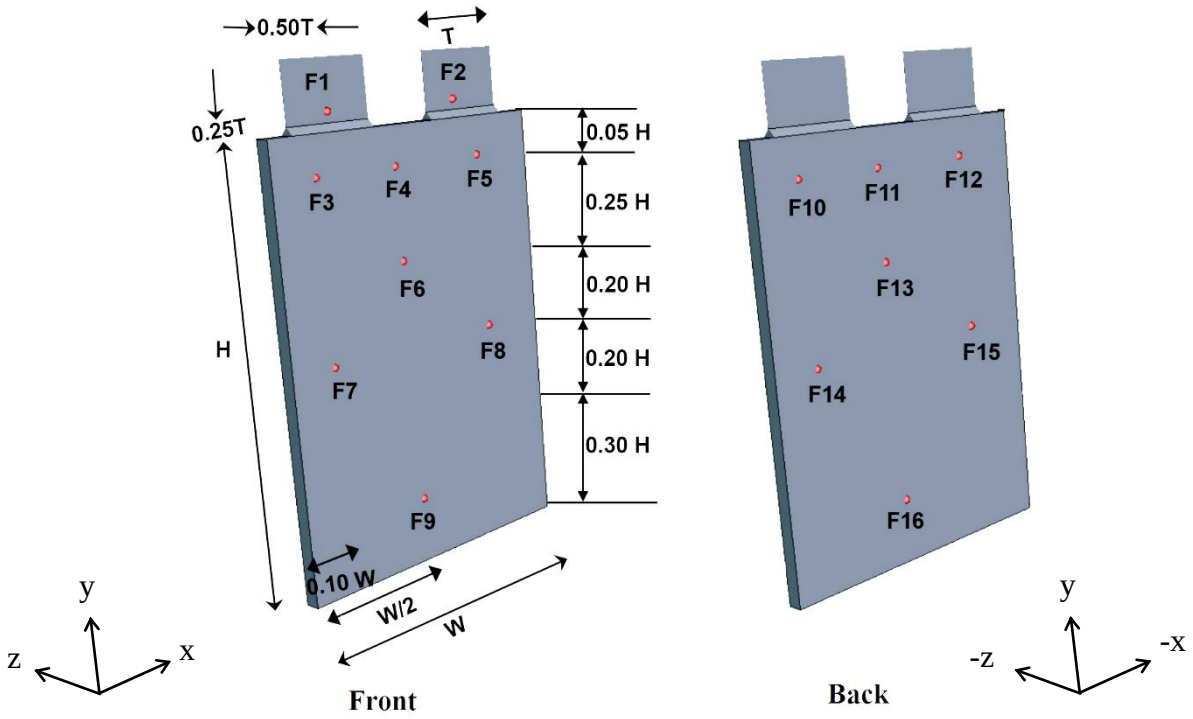

Figure 1: Thermocouple positions on the cell surface

Figure 2

Click here to download Figure(s) - provide separately in addition to within the manuscript file: Figure 2.docx

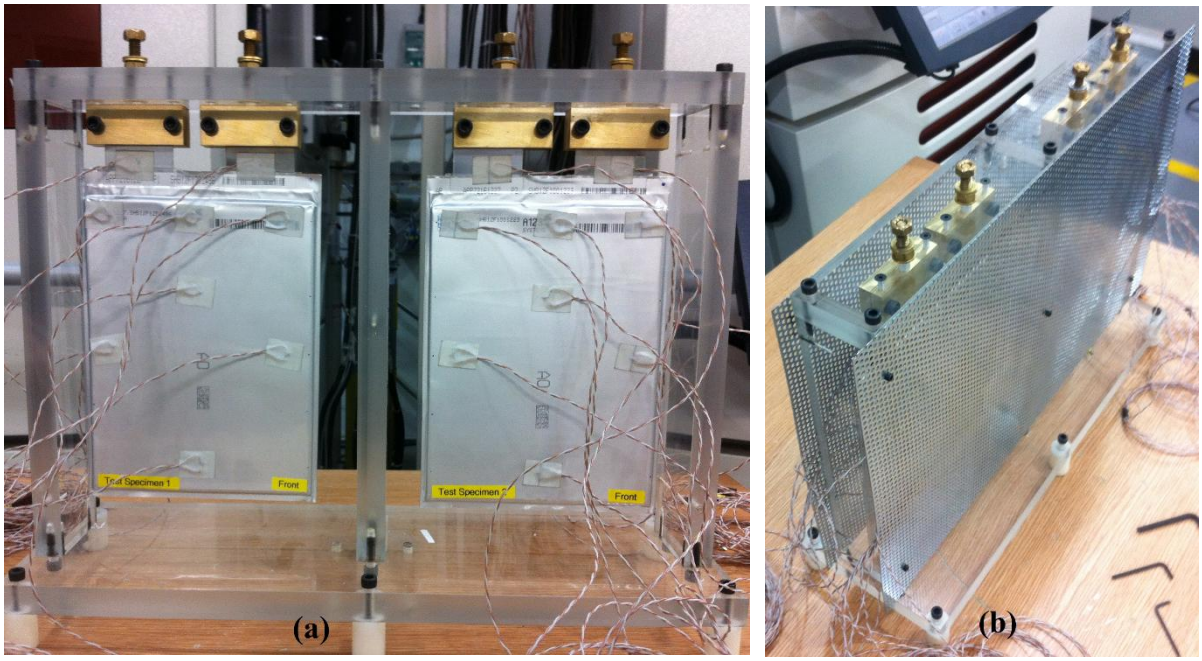

Figure 1: Cell connection with (a) test rig, (b) test rig is covered with a mesh.

Figure 3

Click here to download Figure(s) - provide separately in addition to within the manuscript file: Figure 3.docx

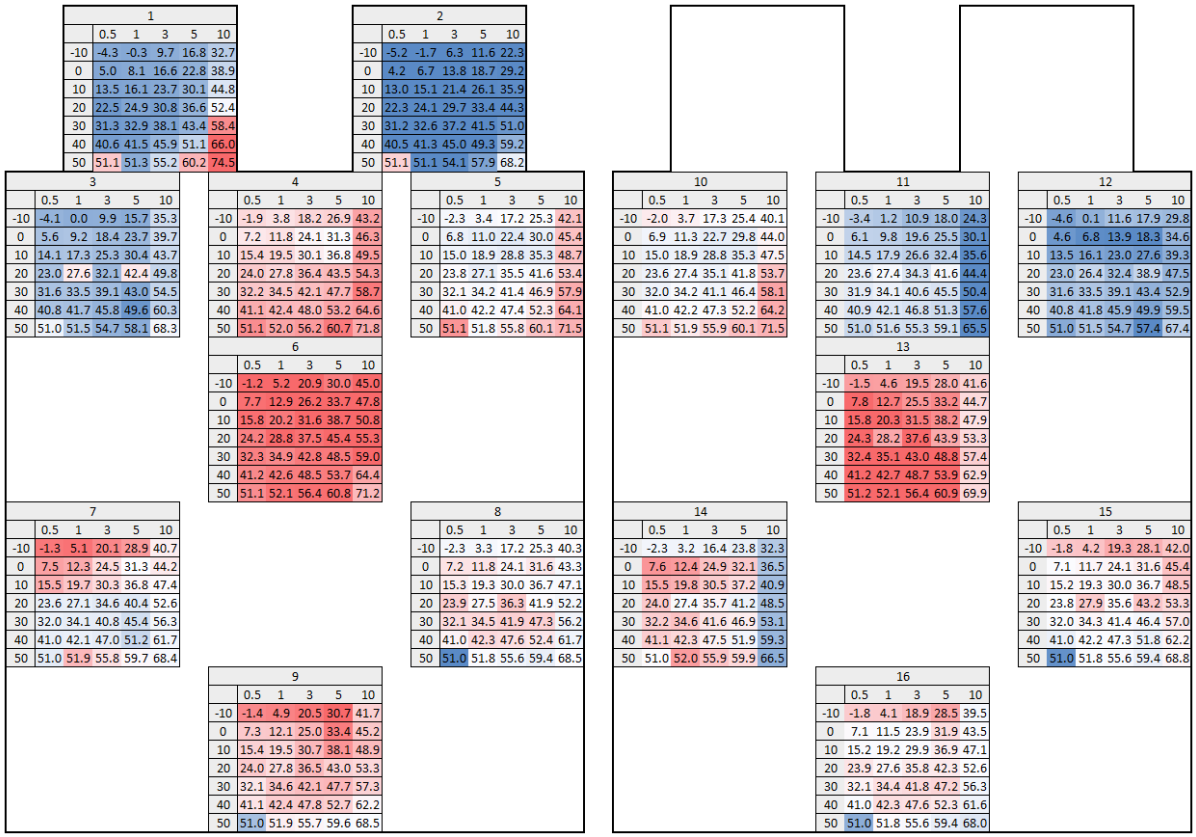

Figure 1: Maximum surface (*X*-*Y*) temperatures for different discharge C-rates (0.5-10C) and ambient conditions (–10˚C to 50˚C). Left: front, right: back of cell. Colour coded as dark blue representing the coldest and dark red representing the hottest thermocouple locations.

Figure 4

Click here to download Figure(s) - provide separately in addition to within the manuscript file: Figure 4.docx

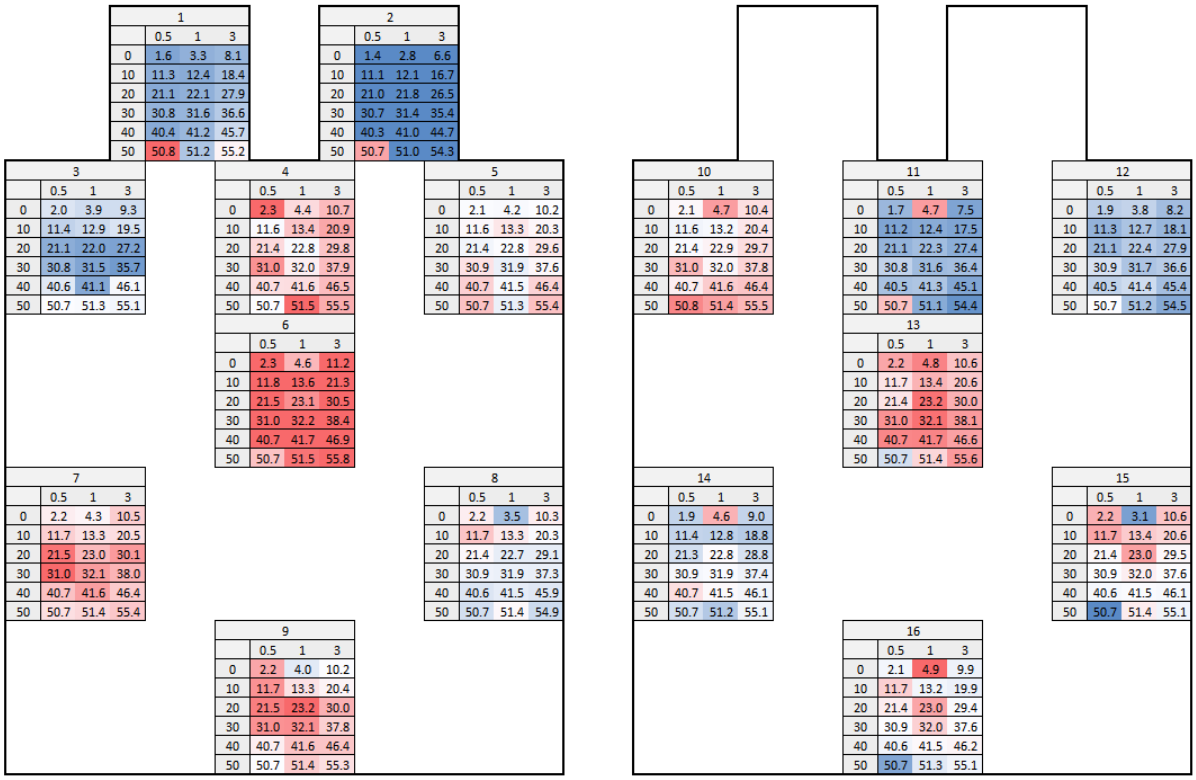

Figure 1: Maximum surface (*X*-*Y*) temperatures for different charge C-rates (0.5-3C) and ambient conditions (0˚C-50˚C). Left: front, right: back of cell. Colour coded as dark blue representing the coldest and dark red representing the hottest thermocouple locations.

Figure 5

Click here to download Figure(s) - provide separately in addition to within the manuscript file: Figure 5.docx

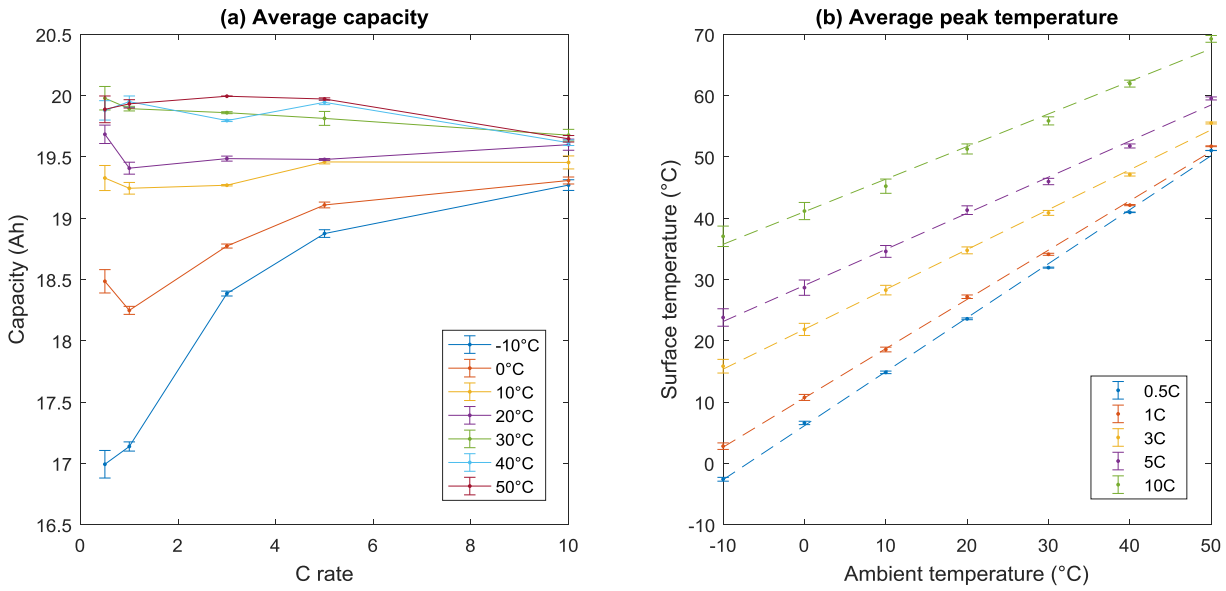

Figure 1: (a) Average capacity vs C rate, (b) Average cell surface peak temperature vs ambient temperature (Error bars represent ±SE)

Figure 6

Click here to download Figure(s) - provide separately in addition to within the manuscript file: Figure 6.docx

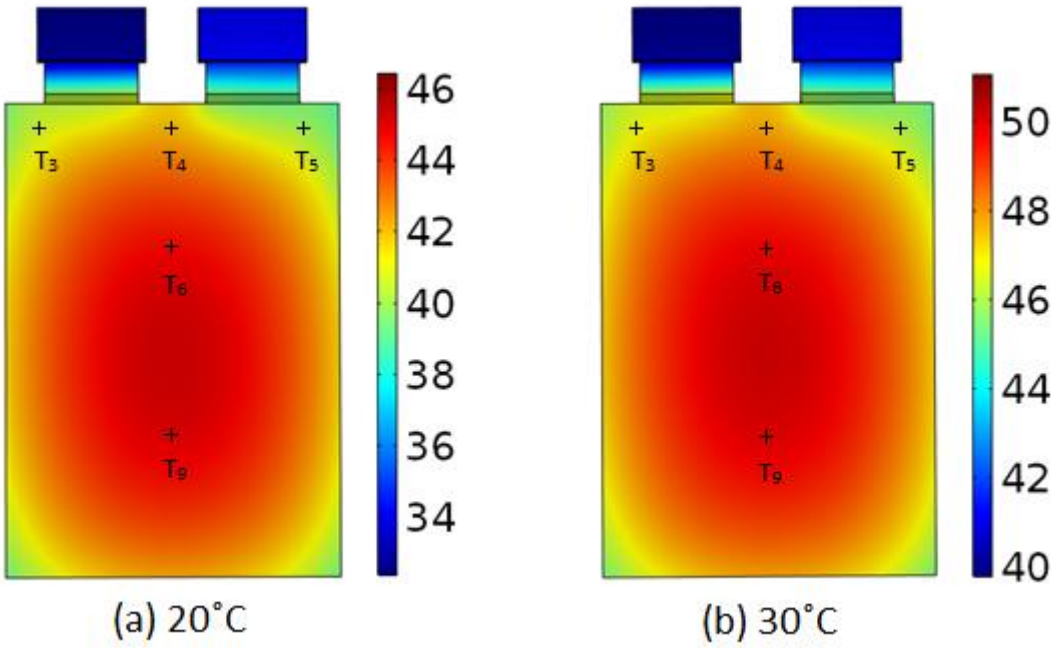

Figure 1: Thermal model temperature distribution at the end of 5C discharge at (a) 20˚C and (b) 30˚C ambient temperature (colour scale in ˚C)

Figure 7

Click here to download Figure(s) - provide separately in addition to within the manuscript file: Figure 7.docx

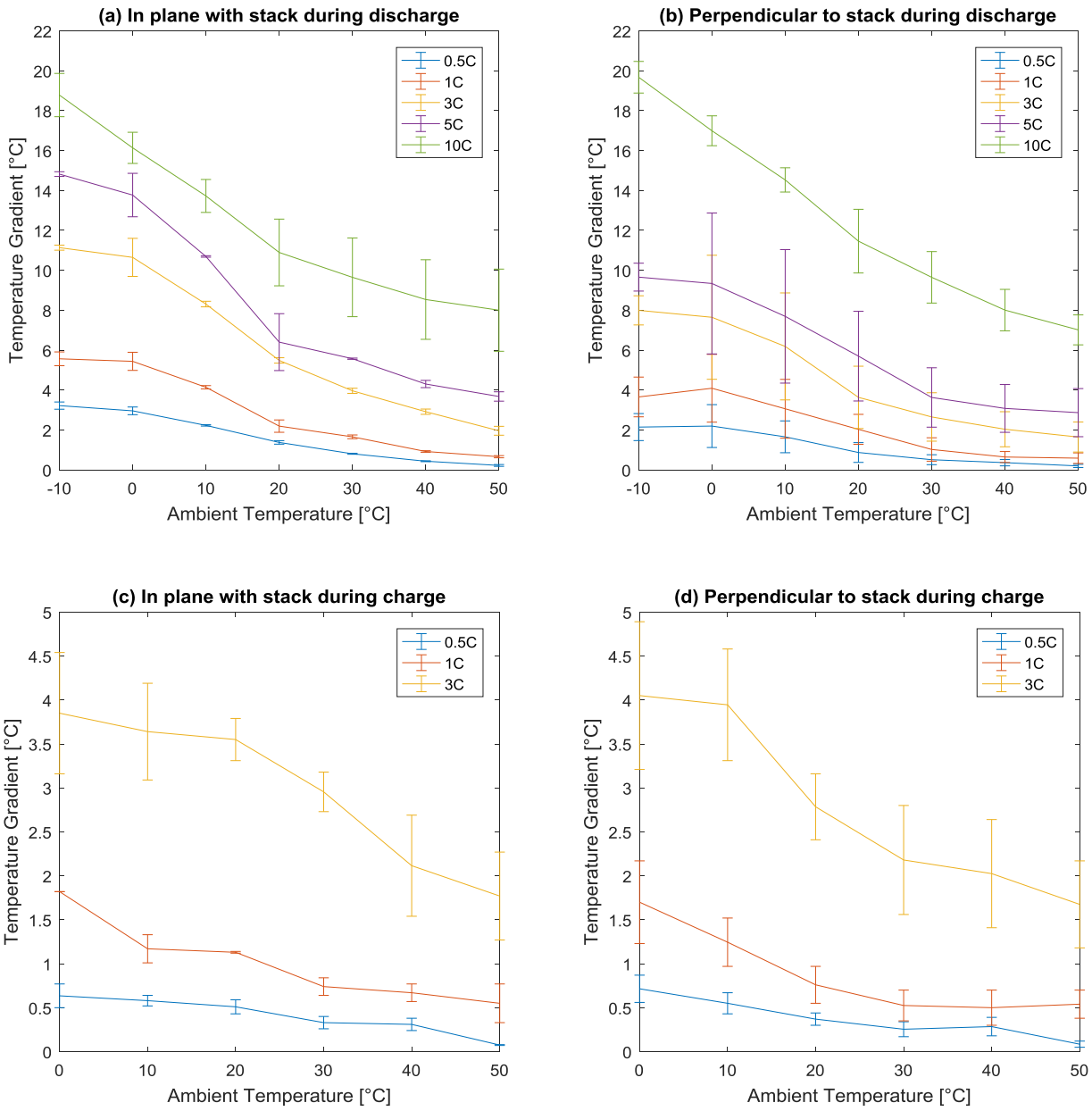

Figure 1: Average maximum cell temperature gradient (excluding tabs) for different C-rates and ambient conditions (Error bars represent ± SE)

Figure 8

Click here to download Figure(s) - provide separately in addition to within the manuscript file: Figure 8.docx

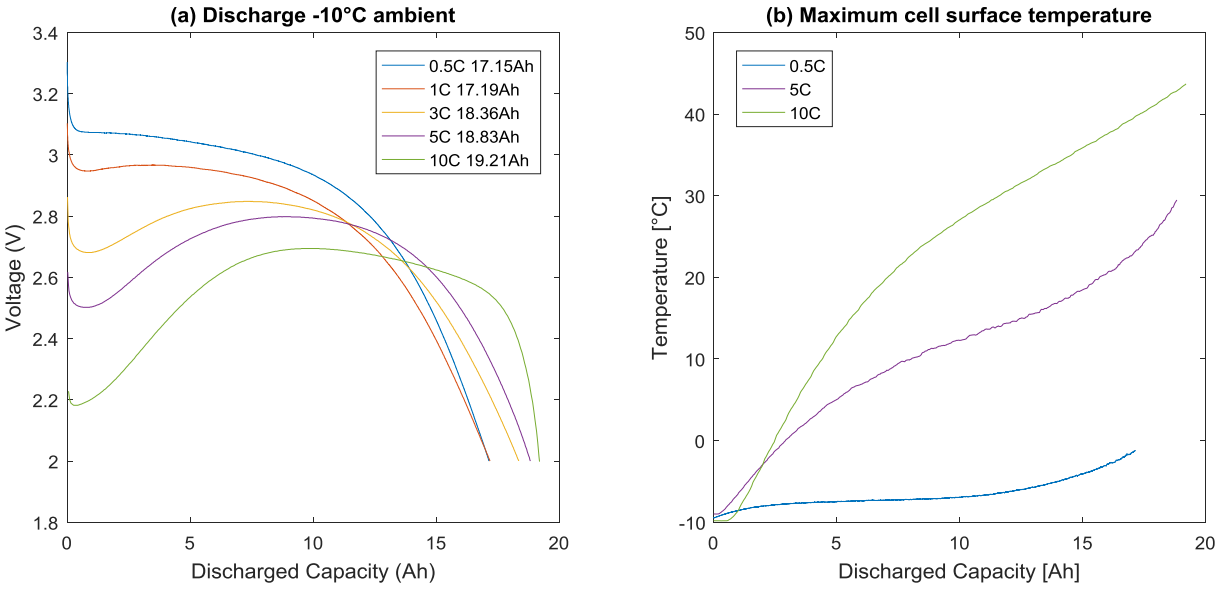

Figure 1: (a) Cell voltage vs capacity at -10°C ambient, (b) Maximum temperature on cell surface during discharge test at -10°C ambient

Figure captions:

Figure 1: Thermocouple positions on the cell surface

Figure 2: Cell connection with (a) test rig, (b) test rig is covered with a mesh.

Figure 3: Maximum surface (*X*-*Y*) temperatures for different discharge C-rates (0.5-10C) and ambient conditions (–10˚C to 50˚C). Left: front, right: back of cell. Colour coded as dark blue representing the coldest and dark red representing the hottest thermocouple locations.

Figure 4: Maximum surface (*X*-*Y*) temperatures for different charge C-rates (0.5-3C) and ambient conditions (0˚C-50˚C). Left: front, right: back of cell. Colour coded as dark blue representing the coldest and dark red representing the hottest thermocouple locations.

Figure 5: (a) Average capacity vs C rate, (b) Average cell surface peak temperature vs ambient temperature (Error bars represent ±SE)

Figure 6: Thermal model temperature distribution at the end of 5C discharge at (a) 20˚C and (b) 30˚C ambient temperature (colour scale in ˚C)

Figure 7: Average maximum cell temperature gradient (excluding tabs) for different C-rates and ambient conditions (Error bars represent ± SE)

Figure 8: (a) Cell voltage vs capacity at -10°C ambient, (b) Maximum temperature on cell surface during discharge test at -10°C ambient

Table captions:

Table 1: Cell discharge (D) and charge (C) matrix with temperature and C rate

Table 2: Average peak temperature rise (˚C ± SE) for discharge

Table 3: Measured and thermal model temperature at the end of 5C discharge